Remote Sensing of Environment 199 (2017) 107–119

Contents lists available at ScienceDirect

Remote Sensing of Environment

journal homepage: www.elsevier.com/locate/rse

Improving Fmask cloud and cloud shadow detection in mountainous area for Landsats 4–8 images

Shi Qiu [a], Binbin He [a,b,*], Zhe Zhu [c,**], Zhanmang Liao [a], Xingwen Quan [a]

[a] School of Resources and Environment, University of Electronic Science and Technology of China, Chengdu, Sichuan 611731, China
[b] Center for Information Geoscience, University of Electronic Science and Technology of China, Chengdu, Sichuan 611731, China
[c] Department of Geosciences, Texas Tech University, Lubbock, TX 79409, USA

ARTICLE INFO

Article history:
Received 20 October 2016
Received in revised form 16 June 2017
Accepted 7 July 2017
Available online xxxx

Keywords:
Cloud
Cloud shadow
Fmask
MFmask
Landsat
Mountainous area
DEM

ABSTRACT

We developed a new algorithm called MFmask (Mountainous Fmask) for automated cloud and cloud shadow detection for Landsats 4–8 images acquired in mountainous areas. The MFmask algorithm, built upon the success of the Fmask algorithm (Zhu and Woodcock, 2012; Zhu et al., 2015), is designed for cloud and cloud shadow detection in mountainous areas, where the Fmask algorithm is not performing well. The inputs of the MFmask algorithm include Landsat Top of Atmosphere (TOA) reflectance, Brightness Temperature (BT), and Digital Elevation Models (DEMs). Compared to Fmask, MFmask can separate water and land pixels better in mountainous areas with the aid of DEMs. Moreover, MFmask produces better cloud detection results than Fmask in mountainous areas after BT is linearly normalized by DEMs. To provide more accurate cloud shadow detection in mountainous areas, MFmask uses a double-projection approach to better predict cloud shadow shape on slope side. Additionally, MFmask applies a topographic correction to remove terrain shadows and estimates cloud base height with neighboring clouds. Both will reduce the possibility of cloud and cloud shadow mismatch and increase cloud shadow detection accuracy for places with large topographic gradient. To test the performance of the proposed MFmask algorithm, a total of 67 Landsat images acquired in mountainous areas from different parts of the world were selected for assessing the accuracy of cloud detection, in which 15 of them were used for assessing the accuracy of cloud shadow detection. Compared with Fmask, MFmask can provide substantial improvements in cloud and cloud shadow detection accuracies for places with large topographic gradient and also work well for relatively flat terrain.

1. Introduction

Landsat images have been widely used in mapping and monitoring natural resources (Colstoun et al., 2003; Fisher et al., 2016; Gao et al., 2015). In 2008, the free access policy of the Landsat data has promoted many time series related applications (Cohen et al., 2010; Huang et al., 2010b; Kennedy et al., 2010; Schroeder et al., 2011; Zhu et al., 2016). Nevertheless, many Landsat images are inevitably covered by clouds and their shadows (Asner, 2001; Ju and Roy, 2008), which limit their use (Irish et al., 2006). The presence of clouds and their shadows will decrease the robustness of geophysical parameters retrieval (He et al., 2013; Quan et al., 2015), impact data fusion (Gao et al., 2006; Zhu et al., 2010), increase errors in land cover classification (Li et al., 2012; Yuan et al., 2005), and cause false positive errors in change detection (Coulter et al., 2016; Hermosilla et al., 2015).

Recently, many cloud detection algorithms have been developed for Landsat images (Choi and Bindschadler, 2004; Hagolle et al., 2010; Huang et al., 2010a; Irish, 2000; Irish et al., 2006; Jin et al., 2013; Roy et al., 2010; Wang et al., 1999; Wilson and Oreopoulos, 2013; Zhang et al., 2002; Zhu and Woodcock, 2012; Zhu et al., 2015), among which the Fmask (Function of mask) algorithm has shown relatively better performance in operational cloud detection than the other algorithms (Foga et al., 2017), and it can also detect cloud shadow and snow. The Fmask algorithm has been widely used and has been successfully integrated into the Landsat surface reflectance Climate Data Record (CDR) and Level 1 Quality Assessment (QA) band provided by the U.S. Geological Survey (USGS) Earth Resources Observation and Science (EROS) Center.

Although the Fmask algorithm performs well for Landsat images in most cases, it has some issues in mountainous areas. First, Fmask detects cloud over land and water separately, but the water test is not always accurate. For example, the Fmask algorithm uses a simple water test of Normalized Difference Vegetation Index (NDVI) and the Top of Atmosphere (TOA) reflectance of Near Infrared (NIR) band to divide all pixels into land and water pixels, which may include terrain shadows as water

* Correspondence to: B. He, School of Resources and Environment, University of Electronic Science and Technology of China, Chengdu, Sichuan 611731, China.
** Corresponding author.
E-mail addresses: binbinhe@uestc.edu.cn (B. He), zhe.zhu@ttu.edu (Z. Zhu).

http://dx.doi.org/10.1016/j.rse.2017.07.002
0034-4257/

pixels due to their similar dark spectral signatures (Verpoorter et al., 2012). Second, Fmask assumes that the temperatures from all clear-sky land pixels in one Landsat image are approximately the same, and uses their Brightness Temperature (BT) as the basic temperature to calculate cloud temperature probability. This assumption works well for flat areas, but for mountainous areas, it may not be valid anymore as temperature varies greatly with elevation. What's more, it may lead to more commission errors of clouds in high mountain snow/ice areas because of their similar cold and bright features, subsequently misidentifying cloud shadows as well (Selkowitz and Forster, 2015). Third, the original method for calculating cloud shadow assumes that a cloud and its shadow have a similar shape. This assumption has no problem in flat areas, but for mountainous areas the cloud shadow shape will change substantially if it is casted on steep slopes. Fourth, Fmask searches the location of cloud shadow by calculating the similarity between a cloud and its shadow within an estimated cloud height range. However, sometimes an inaccurate cloud shadow location may be determined when the maximum similarity is reached at other dark features, such as terrain shadows, lakes, and wetlands (Braaten et al., 2015).

To rectify the above limitations, we developed the MFmask (Mountainous Fmask) algorithm to better detect cloud and cloud shadow for Landsats 4–8 images in mountainous areas. Digital Elevation Models (DEMs) are used as the ancillary data for the MFmask algorithm. This new MFmask algorithm can provide: 1) more accurate water detection; 2) better cloud detection; 3) more accurate prediction of cloud shadow shape; and 4) more precise prediction of cloud shadow location. The improvements are especially noticeable for mountainous areas with large topographic gradient.

2. MFmask inputs and validation data

2.1. MFmask inputs

Besides TOA reflectance and BT that are used by the original Fmask algorithm (Zhu and Woodcock, 2012; Zhu et al., 2015), MFmask also uses DEM data. TOA reflectance and BT are derived from the observations of Thematic Mapper (TM), Enhanced Thematic Mapper-Plus (ETM+), and Operational Land Imager/Thermal Infrared Sensor (OLI/TIRS) (in Table 1). DEM data are extracted from the Advanced Spaceborne Thermal Emission and Reflection Radiometer (ASTER) Global DEM Version 2 (NASA JPL, 2009). DEM derivatives, such as slope and aspect, are also used.

2.2. Validation data

A total of 142 Landsat images located in nine latitudinal zones were used to validate Fmask (Zhu and Woodcock, 2012). We downloaded all the 142 Landsat images from the USGS website (https://landsat.usgs.gov/landsat-7-cloud-cover-assessment-validation-data). Most of them were acquired from different locations (Path/Row), but sometimes multiple images may be acquired at different dates from the same location. There are manual cloud masks for all images, but only 26 of them have manual cloud shadow masks. The manual masks were produced by manual visual interpretation of full resolution images in Adobe Photoshop using different combinations of bands by USGS image analysts (Scaramuzza et al., 2012). Meanwhile, 11 of them were randomly examined by all analysts to obtain the approximate error of the manual masks, and the average difference of those manual masks was around 7% (Oreopoulos et al., 2011). The manual masks were designed to systematically cover the full range of global environments and cloud conditions (Irish et al., 2006).

To demonstrate the advantages of MFmask in mountainous regions, we selected the images where DEMs differ more than 500 m, which gives us 67 images and in which 17 of them also have cloud shadow masks. We further excluded two Landsat images in cloud shadow analysis, due to the large omission or commission errors in the manual cloud shadow masks. Therefore, we used 67 images for assessing the accuracy of cloud detection, and 15 images for assessing the accuracy of cloud shadow detection (Fig. 1). The average elevation difference of all the 67 images is approximately 1.52 km, in which most of the elevation differences are less than 2 km, and only 9 images with elevation differences more than 2 km (Fig. 2). Moreover, the cloud cover percentages among the 67 images also vary substantially, with most of the images having cloud cover around 10%, and the rest of them uniformly distributed between 20% and 100% (Fig. 3).

Table 1
Landsat TM, ETM+, and OLI/TIRS spectral bands. The spectral bands used in the MFmask algorithm are highlighted in bold letters.

Landsat 4–5 TM bands (μm)	Landsat 7 ETM+ bands (μm)	Landsat 8 OLI/TIRS bands (μm)
Band 1 (0.45–0.52)	**Band 1 (0.45–0.515)**	Band 1 (0.43–0.45)
Band 2 (0.52–0.60)	**Band 2 (0.525–0.605)**	**Band 2 (0.45–0.51)**
Band 3 (0.63–0.69)	**Band 3 (0.63–0.69)**	**Band 3 (0.53–0.59)**
Band 4 (0.76–0.90)	**Band 4 (0.75–0.90)**	**Band 4 (0.64–0.67)**
Band 5 (1.55–1.75)	**Band 5 (1.55–1.75)**	**Band 5 (0.85–0.88)**
Band 6 (10.40–12.50)	**Band 6 (10.40–12.50)**	**Band 6 (1.57–1.65)**
Band 7 (2.08–2.35)	**Band 7 (2.09–2.35)**	**Band 7 (2.11–2.29)**
	Band 8 (0.52–0.90)	Band 8 (0.50–0.68)
		Band 9 (1.36–1.38)
		Band 10 (10.60–11.19)
		Band 11 (11.50–12.51)

3. The MFmask algorithm

The MFmask algorithm is developed based on the latest Fmask algorithm (3.3 version; https://github.com/prs021/fmask), and the detailed flowchart of the improvements made by MFmask is shown in Fig. 4. As the original Fmask algorithm has been well documented by Zhu and Woodcock (2012) and Zhu et al. (2015), we will mainly focus on the improvements we have made in this study.

3.1. Water detection

The Fmask algorithm produces a mask for cloud over land and water separately, therefore, we need to classify water pixels before cloud detection is performed. However, the "Water Test" of Fmask relies heavily on two thresholds of NDVI and the NIR band, which may misidentify terrain shadows as water because the spectral response of water is quite similar as terrain shadows (Verpoorter et al., 2012). To classify water pixels more accurately in mountainous areas, MFmask combines a slope threshold with value of 10° with the original "Water Test" (Eq. (1)). The reason why 10° is chosen as the threshold is that the slope of water body is generally less than 10°, but terrain shadows are usually higher (Lu et al., 2011). This minor modification will remove many false positive water pixels (contributed by terrain shadows) from the final water mask.

$$\text{Water Test} = ((\text{NDVI}<0.01 \text{ and Band NIR}<0.11) \text{ or } (\text{NDVI}<0.1 \text{ and Band NIR}<0.05)) \text{ and Slope}<10^{\circ} \quad (1)$$

3.2. Cloud detection

The Fmask algorithm estimates the cloud probability of land pixels by integrating the temperature probability, which is calculated by using the lower level (T_{low}) and the upper level (T_{high}) of the clear-sky land pixels' BT within the entire image (Eq. (2)). The clear-sky pixels are identified by the pass one of Fmask, which combines several spectral tests to select the pixels that 100% cloud-free in the Landsat image. T_{low} and T_{high} are calculated from the 17.5 and 82.5 percentile of clear-sky

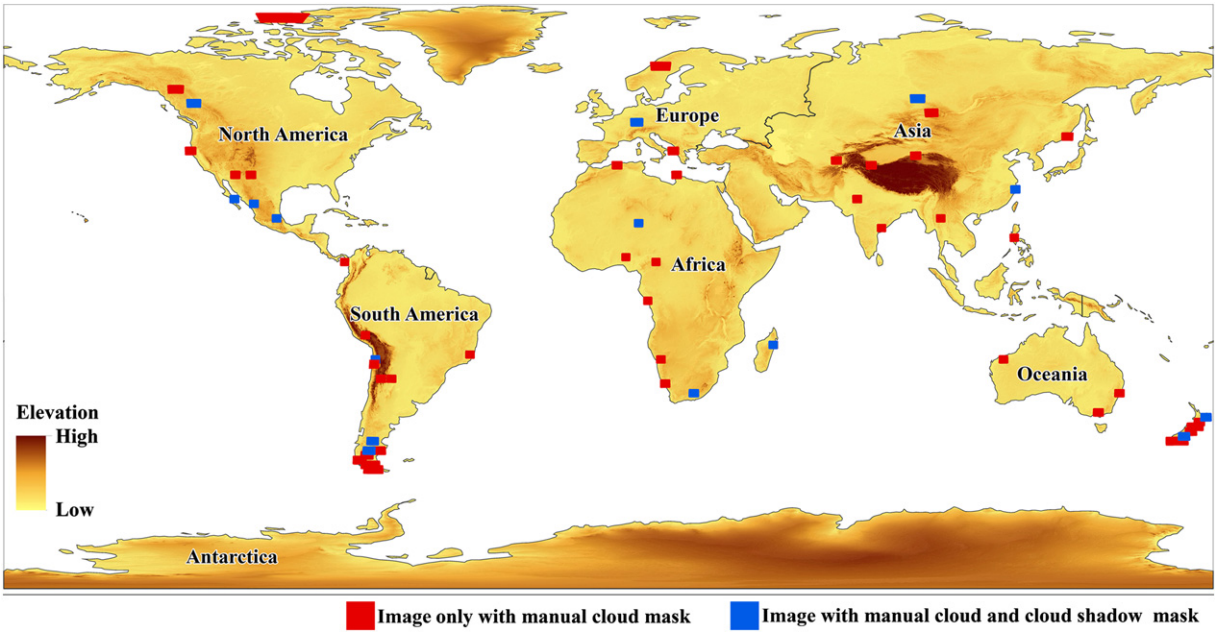

Fig. 1. Distribution of Landsat images for validating the MFmask algorithm. The red rectangles show the coverage of Landsat images with manual cloud masks, and the blue rectangles show the coverage of Landsat images with both manual cloud and cloud shadow masks. The elevation background was rendered using the Global 30 Arc-Second Elevation (GTOPO30) data (https://lta.cr.usgs.gov/GTOPO30). (For interpretation of the references to color in this figure legend, the reader is referred to the web version of this article.)

land pixels' BT, which provide the temperature interval for clear-sky land pixels (Zhu and Woodcock, 2012). Finally, clouds over land can be identified by a dynamic threshold from the cloud probability of all clear-sky land pixels.

$$lTemperatrue\_Prob = (T_{high} + 4 - BT)/(T_{high} + 4 - (T_{low} - 4)) \quad (2)$$

The original Fmask has accounted for the brightness temperature variation at scene level, but it is not sufficient for mountainous areas where the environmental temperature can widely vary with large elevation changes. The environmental temperature commonly indicates air temperature, but it is also affected by surface temperature (Sandholt et al., 2002). As the environmental temperature is often negatively related to elevation, clear-sky land pixels with high elevations are usually having lower temperature than the pixels with relatively low elevations (Lookingbill and Urban, 2003), which makes a scene-based threshold problematic. To overcome this problem, we used BT as a proxy for the environmental temperature and built a linear lapse rate model to normalize it based on the DEM, which assumes that the temperature linearly changes with the elevation (Lookingbill and Urban, 2003). The BT normalization processes are introduced in Section 3.2.1 and Section 3.2.2.

3.2.1. Calculation of lapse rate

To establish the temperature-elevation relationship, MFmask utilizes a simple linear lapse rate model (Eq. (3)) (Lookingbill and Urban, 2003).

$$T(x,y) = t_0 + \gamma \cdot E(x,y) + \varepsilon \quad (3)$$

where,

T is the measured BT in Celsius degrees,

E is the elevation in kilometers,

(x,y) is a pixel's location for the Landsat image,

γ is the slope, which represents the temperature lapse rate in Celsius degrees per kilometer,

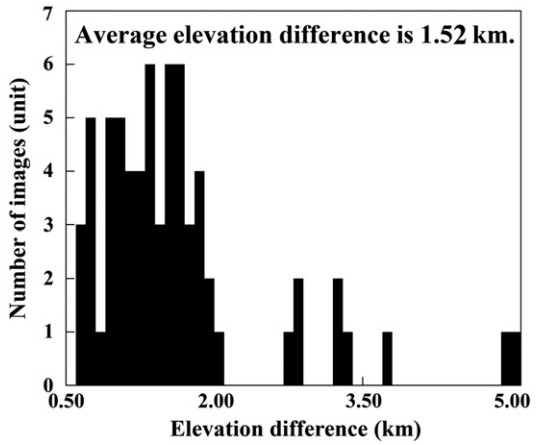

Fig. 2. Histogram of the elevation differences of the 67 reference images.

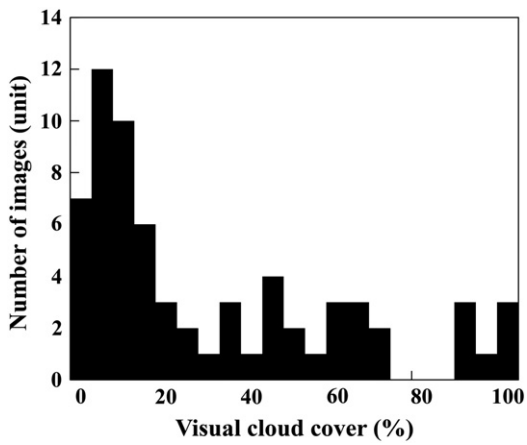

Fig. 3. Histogram of the visual cloud cover percentage of the 67 reference images.

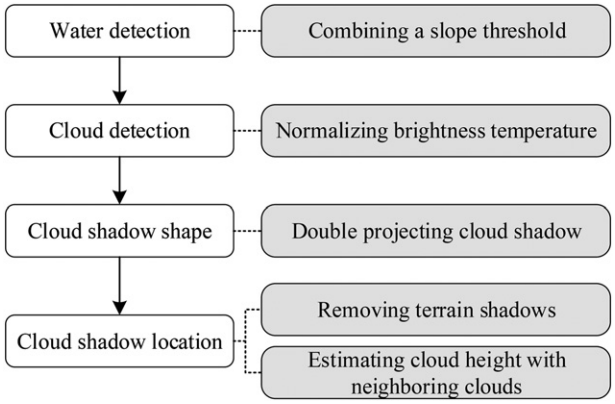

Fig. 4. The flowchart of the improvements made by the MFmask algorithm.

t_0 is the intercept, which represents the temperature in Celsius degrees at 0 elevation,

ε is the error of regression.

The lapse rate will be estimated based on the clear-sky land pixels previously identified by the original Fmask. To exclude other environmental influences that usually make clear-sky pixel temperatures colder or warmer (e.g., snow/ice and urban heat island), MFmask only selects those pixels between the lower level (17.5 percentile) and the upper level (82.5 percentile) of clear-sky land temperatures as the candidate pixels for estimating the linear model. Among all the clear-sky land pixels, we employed a stratified random sampling approach (randomly select equal number of clear-sky land pixels in every 0.3 km along elevation) to obtain a total of 50,000 pixels to calculate the temperature lapse rate γ in linear regression. The reason for choosing 0.3 km is that the variability of all clear-sky land pixels' BT in each subgroup is lowest when they are grouped in every 0.3 km (Fig. 5). At the same time, to reduce the redundancy of those selected pixels, we also integrated a 450 m distance rule into this sampling process (Munroe et al., 2004).

As an example of the linear regression analysis (Fig. 6a), there are many clear-sky land pixels identified within the Landsat 7 ETM+ image acquired at Path 36/Row 37 on May 1, 2001. Based on the sample pixels, a linear regression model can be estimated (Fig. 6a), and the slope represents the temperature lapse rate γ within the image ($\gamma = -5.39\ °C\ km^{-1}$). In this case, R^2 is relatively low because the spatial variation of temperature may be affected by many physiographic factors,

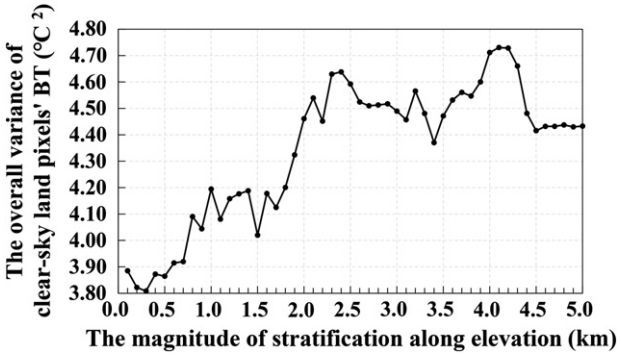

Fig. 5. The selection of stratified elevation by analyzing all 67 reference images. For each stratification of elevation, the overall variances of clear-sky land pixels' BT were calculated by the mean of variances of all clear-sky land pixels' BT from all 67 reference images. Note that the lowest variance is achieved when the subgroups are stratified in every 0.3 km.

such as elevation, surface condition, air moisture content, and wind speed (Kattel et al., 2013).

In some specific cases, when other physiographic factors have greater impacts on temperature variation than elevation, the lapse rate γ derived from regression may not be real. Therefore, when the estimated lapse rate γ is larger than 0 °C km^{-1} or the linear regression model is not statistical significance at 0.05 level, MFmask will set γ to be 0 °C km^{-1}, which means the effect of elevation change on temperatures is not significant, and the original Fmask method will be adopted.

3.2.2. Temperature normalization

To reduce the temperature variability caused by elevation change, MFmask normalizes the BT of all pixels onto a "reference plane", which is defined as a horizontal plane located at the lowest elevation of the Landsat image. The lowest elevation can be obtained from DEMs. When the lapse rate γ has been calculated using the clear-sky land pixels (Section 3.2.1), the BT of all pixels can be linearly normalized by Eq. (4).

$$NT(x, y) = T(x, y) - \gamma \cdot (E(x, y) - E_{ref}) \quad (4)$$

where,

NT is the normalized BT in Celsius degrees,

E_{ref} is the reference plane's elevation in kilometers.

As a result of temperature normalization using the lapse rate γ (Fig. 6b), the clear-sky land pixels normalized by MFmask were plotted to show the relationship between temperature and elevation within the Landsat 7 ETM+ image acquired at Path 36/Row 37 on May 1, 2001. Fig. 6a shows that the temperature of clear-sky land pixels decreases with the increasing elevation, while after normalization, there is no obvious relationship between the elevation and the temperature for the clear-sky land pixels (Fig. 6b).

Since the normalized BT can reduce the influence from elevation change, MFmask takes it as input to detect cloud over land.

3.3. Cloud shadow shape

The Fmask algorithm predicts cloud shadow shape assuming that the shapes of cloud objects are similar with their shadows. The cloud objects are derived by segmenting the cloud layer, that is, all cloud pixels 8-connected to each other are identified as one cloud object (Zhu and Woodcock, 2012). However, the assumption may not be valid when the cloud shadows are projected on steep slopes. Fig. 7 shows the cloud shadow shape observed in the image would be quite different from the shape of the corresponding cloud when a cloud shadow is projected on a slope side. Note that the location of real cloud shadow is also slightly shifted compared with the flat reference plane. To account for this shape change, MFmask applies a "double-projection" approach with integration of DEMs to better predict cloud shadow shape in Landsat image. The basic idea of this double-projection approach is that based on the geometric relationship between a cloud and its shadow, we can firstly project the cloud shadow onto the reference plane (hereafter called "referenced cloud shadow"), and later the cloud shadow in Landsat image (hereafter called "imaged cloud shadow") can be obtained by back projecting the referenced cloud shadow onto the DEM map along the sunlight direction.

The first projection directly projects cloud shadow onto the reference plane similarly as Fmask (Zhu and Woodcock, 2012), except that the cloud base height (H_c) used in MFmask is relative to the horizontal reference plane rather than the real surface (Fig. 8). This projection is based on the solar-sensor geometry (Fig. 8): the sensor viewing zenith angle (θ_v), the sensor viewing azimuth angle (φ_v), the solar zenith angle (θ_s), the solar azimuth angle (φ_s), and the cloud base height (H_c). Note that the first four factors are already known. At the same time, we followed the Fmask method to estimate the cloud base height (H_c), but used the normalized BT and took account of DEMs (Eq. (5)).

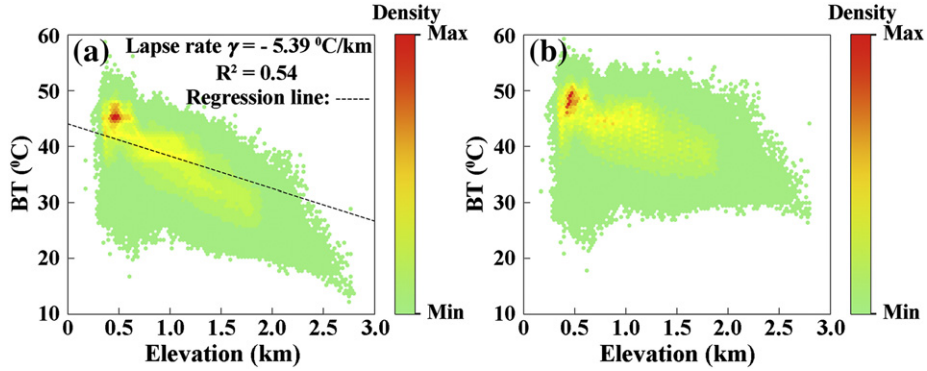

Fig. 6. Temperature normalization for a Landsat 7 ETM + image acquired at Path 36/Row 37 on May 1, 2001 (BT: Brightness Temperature). (a) The original BT versus the elevation for all clear-sky land pixels in the Landsat image. A linear regression model ($\gamma = -5.39\ ^{\circ}C\ km^{-1}$, $R^2 = 0.54$) can be estimated based on the stratified samples. (b) The normalized BT versus the elevation for all clear-sky land pixels. The colors indicate the density of the scatter plot. (For interpretation of the references to color in this figure legend, the reader is referred to the web version of this article.)

Based on the five variables, the referenced cloud shadow can be calculated by using the discretization projection (Eqs. (6) and (7)) for pixels of each cloud object (the first projection). Note that the position of clouds in Landsat image (observed by the sensor) will be different from the position of real clouds.

$$H_c = \left\{ \begin{array}{ll} \text{from} & \max\left(0.2 + \Delta E_c, \left(NT_{low} - 4 - T_{cloud\_base}\right)/9.8\right) \\ \text{to} & \min\left(12 + \Delta E_c, \left(NT_{high} + 4 - T_{cloud\_base}\right)\right) \end{array} \right\} \text{km} \quad (5)$$

where,

NT_{low} and NT_{high} represent the lower (17.5 percentile) and upper (82.5 percentile) level of the clear-sky land pixels' normalized BT, respectively,

ΔE_c represents the elevation difference between cloud's underlying surface and the horizontal reference plane (derived from DEMs),

T_{cloud_base} denotes the original BT of cloud object, which is defined in the Fmask algorithm (Zhu and Woodcock, 2012).

$$(x_r, y_r) = (x_c + (H_c - \Delta E_c) \cdot \tan\theta_v \cdot \sin\varphi_v, y_c - (H_c - \Delta E_c) \cdot \tan\theta_v \cdot \cos\varphi_v) \quad (6)$$

$$\left(x_p, y_p\right) = (x_r - H_c \cdot \tan\theta_s \cdot \sin\varphi_s, y_r + H_c \cdot \tan\theta_s \cdot \cos\varphi_s) \quad (7)$$

$$(x_s, y_s) = \left(x_p + H_s \cdot \tan\theta_s \cdot \sin\varphi_s, y_p - H_s \cdot \tan\theta_s \cdot \cos\varphi_s\right) \quad (8)$$

where,

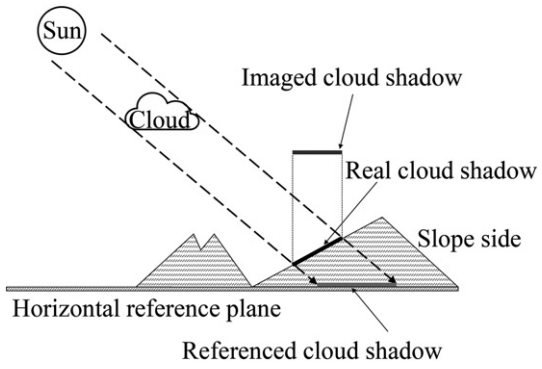

Fig. 7. Illustration of the shape change of cloud shadow on slope side. "Horizontal reference plane" is the horizontal plane located at the lowest elevation of a Landsat image (see Section 3.2.2). "Imaged cloud shadow" is the cloud shadow observed by Landsat. "Real cloud shadow" is the cloud shadow casted on slope side in the actual environment. "Referenced cloud shadow" is the shadow directly projected onto the horizontal reference plane.

θ_v is the sensor viewing zenith angle in degrees,

φ_v is the sensor viewing azimuth angle in degrees,

θ_s is the solar zenith angle in degrees,

φ_s is the solar azimuth angle in degrees,

(x_c, y_c) is the cloud position observed by the sensor (already known in the cloud detection),

(x_r, y_r) is the real cloud position,

(x_p, y_p) is the referenced cloud shadow position (calculated by the first projection),

(x_s, y_s) is the imaged cloud shadow position (calculated by the second projection),

H_c is the cloud base height relative to the horizontal reference plane (calculated by Eq. (5)),

H_s is the height of the imaged cloud shadow relative to the reference plane (derived from DEMs).

The second projection calculates the imaged cloud shadow by back projecting the referenced cloud shadow (calculated from the first projection) onto the DEM map (geometrically registered with Landsat image) along the sunlight direction (Fig. 8). This back projection is based on the simple solar geometry: the solar zenith angle (θ_s), the solar azimuth angle (φ_s), and the imaged cloud shadow height (H_s). Note that the imaged cloud shadow height (H_s) is also relative to the same reference plane, which can be easily calculated by DEM difference. Ideally, the imaged cloud shadow can be predicted from the referenced cloud shadow by Eq. (8). Though the solar zenith angle (θ_s) and the solar azimuth angle (φ_s) are known, the imaged cloud shadow height (H_s) cannot be derived from the corresponding DEM data before determining the imaged cloud shadow position (x_s,y_s). In this case, Eq. (8) cannot be solved directly. Therefore, we projected each pixel of the DEM map (including all pixels of the imaged cloud shadow) onto the reference plane (including all pixels of the referenced cloud shadow) along the sunlight direction following Eq. (8) and constructed a pixel-position relation table between the imaged cloud shadow and the referenced cloud shadow$\{((x_s^k, y_s^k), (x_p^k, y_p^k)), k = 1, \ldots, n\}$, where (x_s^k, y_s^k) is the imaged cloud shadow position of the kth pixel, (x_p^k, y_p^k) is the referenced cloud shadow position of the corresponding kth pixel, and n is the total number of the pixels in image. The imaged cloud shadow can be determined by searching the pixel-position relation table for pixels of each referenced cloud shadow object (the second projection).

3.4. Cloud shadow location

The Fmask algorithm finds cloud shadow from a potential cloud shadow layer by iterating cloud height within a limited range (Zhu and Woodcock, 2012). The locations of cloud shadows are determined by the similarity match between clouds and their shadows. However, for mountainous areas, dark features, such as terrain shadows, lakes,

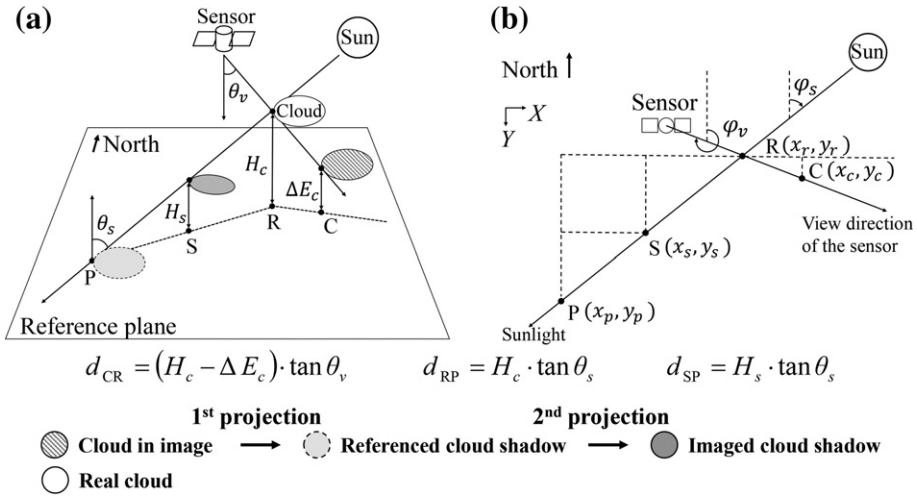

Fig. 8. Illustration of the double-projection for cloud and cloud shadow matching. (a) 3D geometry. (b) 2D geometry projection. Note that the sensor viewing zenith angle (θ_v), the sensor viewing azimuth angle (φ_v), the solar zenith angle (θ_s), and the solar azimuth angle (φ_s) are known. C (x_c,y_c) is the cloud position observed by the sensor. R (x_r,y_r) is the real cloud position. P (x_p,y_p) is the referenced cloud shadow position (first projection). S (x_s,y_s) is the imaged cloud shadow position (second projection). H_c is the cloud base height relative to the horizontal reference plane (calculated by Eq. (5)). ΔE_c is the elevation difference between cloud's underlying surface and the horizontal reference plane (derived from DEMs). H_s is the imaged cloud shadow height relative to the horizontal reference plane (derived from DEMs).

and wetlands, may confuse the Fmask similarity match and result in wrong cloud shadow locations (e.g., early false match). To rectify these limitations, MFmask removes terrain shadows by a topographic correction model and estimates a cloud base height with neighboring clouds to reduce the confusions from other dark features. The details in searching cloud shadow location in MFmask are shown in Fig. 9.

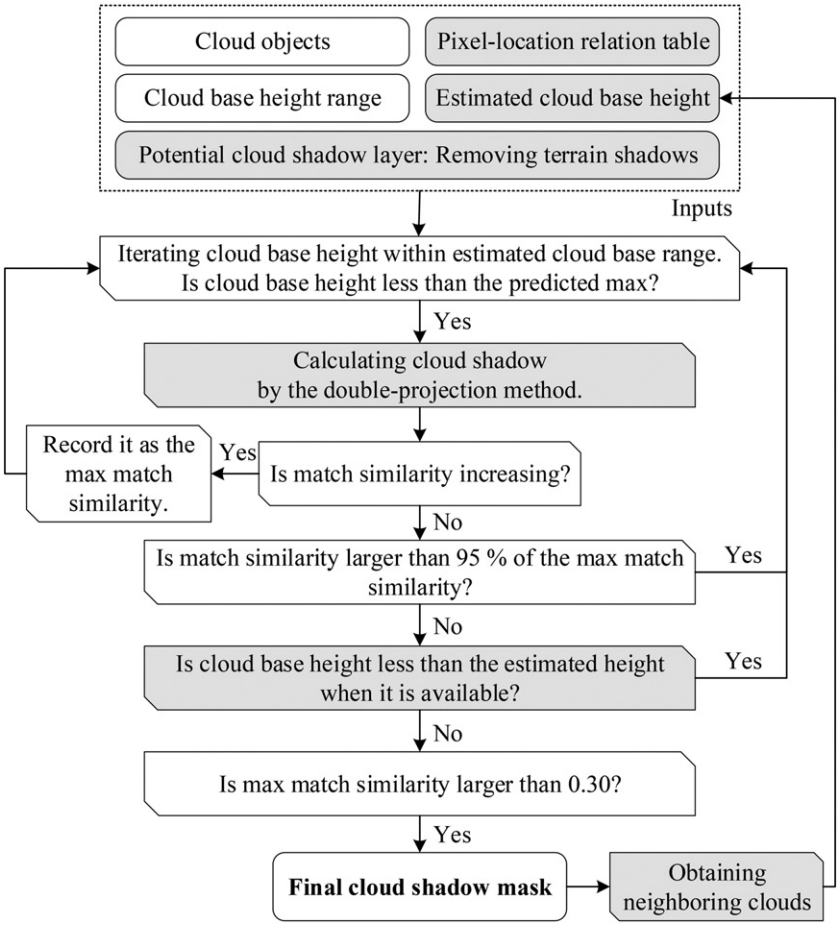

Fig. 9. Flowchart of searching cloud shadow location in MFmask. The gray parts represent the improvements made in the MFmask algorithm.

3.4.1. Remove terrain shadows

We utilized the sun-canopy-sensor with a semiempirical moderator (SCS + C) correction (Soenen et al., 2005) to remove terrain shadows for the NIR and Short Wave Infrared (SWIR) bands. The correction is expressed as follows:

$$\rho' = \rho \cdot \frac{\cos\theta_n \cdot \cos\theta_s + C}{\cos i + C} \quad (9)$$

where,

ρ' is the normalized reflectance,

ρ is the uncorrected reflectance,

θ_n is the terrain slope in degrees,

i is the solar incidence angle in relation to the normal on a pixel,

C is a parameter that can be analogous to the effects of diffuse sky irradiance (Teillet et al., 1982).

The cosine of i is calculated using the following equation:

$$\cos i = \cos\theta_s \cdot \cos\theta_n + \sin\theta_s \cdot \sin\theta_n \cdot \cos(\varphi_s - \varphi_n) \quad (10)$$

where, φ_n is the aspect in degrees.

The solar zenith angle (θ_s) and the solar azimuth angle (φ_s) are known, while all proposed topographic variables (the terrain slope θ_n and the aspect φ_n) are derived from DEMs. The parameter C can be computed by the ratio between intercept and slope of the regression line (Eq. (11)) from the statistical-empirical approach (Teillet et al., 1982). It assumes that there is a linear relationship (Eq. (12)) between uncorrected reflectance ρ and cos i for the clear-sky land pixels generated by the cloud detection (see Section 3.2). The sample pixels used to estimate the empirical parameter C are stratified on the cos i with 0.1 increasement (Reese and Olsson, 2011). The random clear-sky land pixels within each cos i strata have equal allocation (a total of 50,000 pixels).

$$C = \frac{a}{b} \quad (11)$$

$$\rho = a + b \cdot \cos i \quad (12)$$

3.4.2. Estimate cloud base height with neighboring clouds

Although the terrain shadows have been removed, the potential cloud shadow layer may still include other dark features, such as lakes and wetlands. To further reduce their impacts on the calculation of cloud shadow locations, the MFmask algorithm estimates a cloud base height with neighboring clouds and applies it to assist cloud shadow detection, assuming neighboring cloud objects have similar cloud base heights.

Normally, the height of the neighboring clouds should be close to each other, and Berendes et al. (1992) suggested that the standard deviation of cloud heights is within a small range (from 0.1 to 0.15 km). Therefore, the MFmask algorithm uses the statistics of heights of the previously calculated neighboring clouds (close in distance) to estimate the new cloud height. The neighboring clouds can be obtained by calculating the distances between the centers of two cloud objects. However, sometimes the obtained neighboring clouds are relatively dispersed or some clouds are substantially higher than the clouds nearby (e.g., cirrus clouds), the estimated cloud height from this method will be no longer accurate. Therefore, MFmask will only estimate cloud height when the standard deviation of the neighboring clouds is less than 1 km.

The estimated cloud base height is determined by the upper level (82.5 percentile) of the matched heights of 14 neighboring clouds. The upper level (82.5 percentile) is used to exclude the overestimated cloud heights. The number of neighboring cloud objects was determined by the sensitivity analysis (Fig. 10). Considering that the cloud shadow producer's accuracy is more important than the user's accuracy, we selected the one (14 neighboring cloud objects) with the highest average producer's accuracy based on a set of 15 mountainous Landsat reference images (see Section 2.2 for details). To further ensure that the new cloud is not far from its obtained neighboring clouds, the estimated cloud height is available only when it is between the previously estimated minimum height and the maximum height (Eq. (5)).

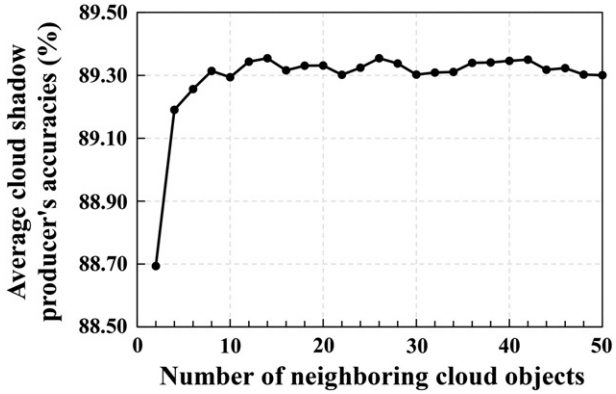

Fig. 10. An example of choosing the number of neighboring clouds based on sensitivity analysis. Note that 14 neighboring cloud objects achieved the highest average producer's accuracy in cloud shadow detection.

The estimated cloud height is used to assist the prediction of cloud shadow location. In the MFmask algorithm, the search of cloud shadow location will not stop until it reaches this estimated cloud height. The cloud shadow is matched with cloud when the similarity gets maximum during the whole search process (Fig. 9). If there are multiple maximum similarities, MFmask selects the one with the cloud height closest to the estimated cloud height. Note that if the estimated height is not available, the location of cloud shadow will be determined by the original Fmask's searching rule.

4. MFmask results and accuracy assessment

4.1. MFmask results

As the improvements are particularly noticeable for mountainous regions, we displayed MFmask results for some typical mountainous images that have large topographic changes. By comparing the results between MFmask and Fmask visually (Fig. 11a, b, c, d, and e), MFmask shows better performance in detecting cloud and cloud shadow in mountainous areas. Fig. 11a shows the results of a Landsat 7 ETM+ image located in the Himalayas Mountains with large elevation changes and covered with thick cumulus clouds. Compared with Fmask, MFmask shows better cloud detection in the areas with low elevation (less omission errors). Fig. 11b shows the results of a Landsat 7 ETM+ image located in the Alps Mountains, where thin clouds cover the areas with low elevation. The results also demonstrate that MFmask results are more accurate in capturing some of the thin clouds located at the lower side of the image. Fig. 11c shows the results of one Landsat 7 ETM+ image located in the Caucasus Mountains, with a mixture of thin clouds and bright mountain snow/ice. Both algorithms show large commission errors in cloud and cloud shadow detection, however, the commission errors in MFmask are substantially reduced compared with Fmask. Additionally, Fig. 11d shows the results of a Landsat 7 ETM+ image located in the Longmen Mountains, where there are large terrain variations in the southwest. By checking the subset masks (see red arrows), we can see that MFmask identifies the cloud shadows more accurately than Fmask. Finally, Fig. 11e shows the results of a Landsat 7 ETM+ image located in the Air Mountains. In this location, there are large areas of volcanic outcrops with dark features. Fmask fails to capture the corresponding shadows for clouds over the large dark features. However, MFmask correctly identifies the shadows of those clouds (see red arrows).

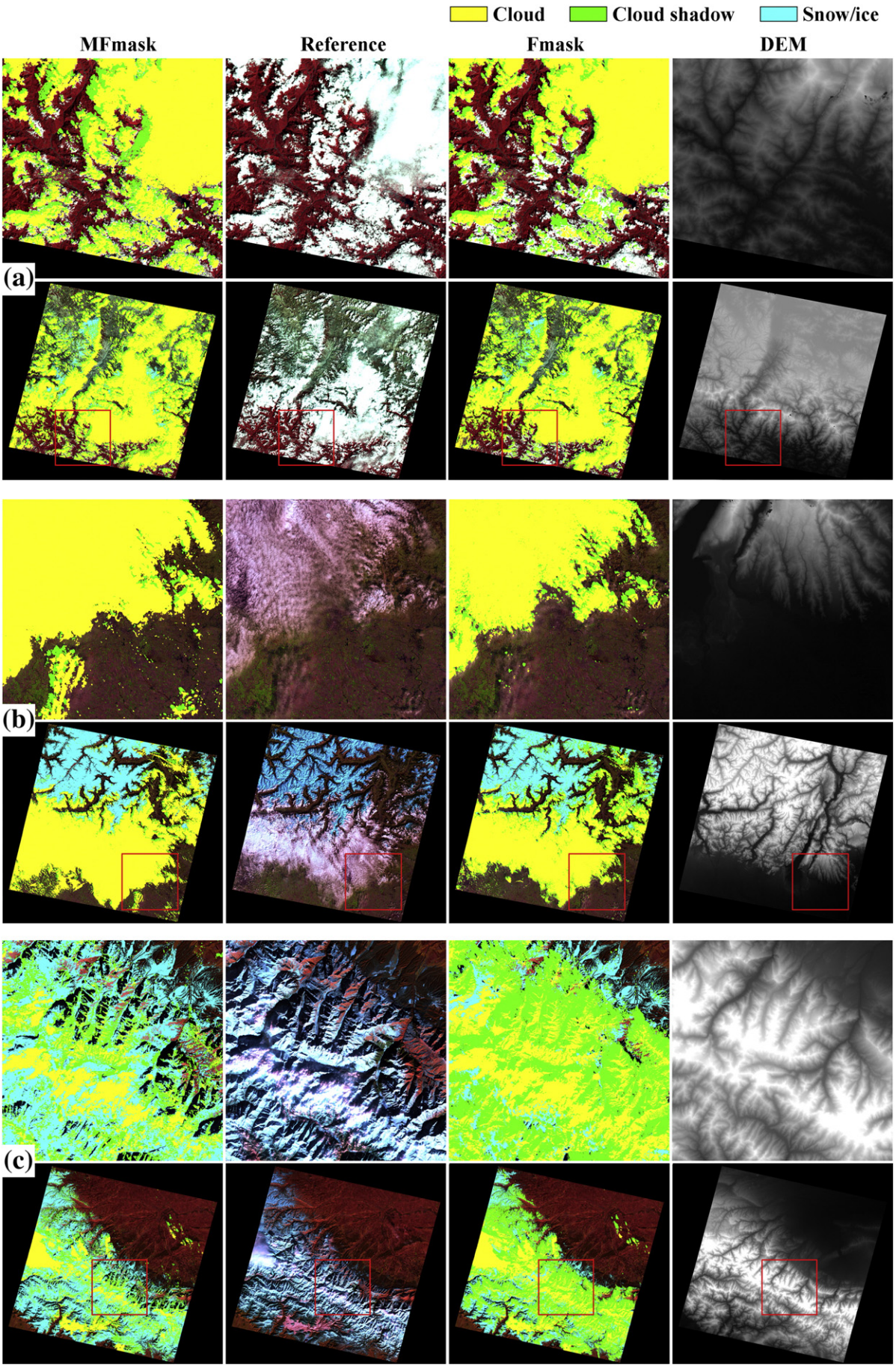
Cloud
Cloud shadow
Snow/ice
MFmask
Reference
Fmask
DEM
(a)
(b)
(c)

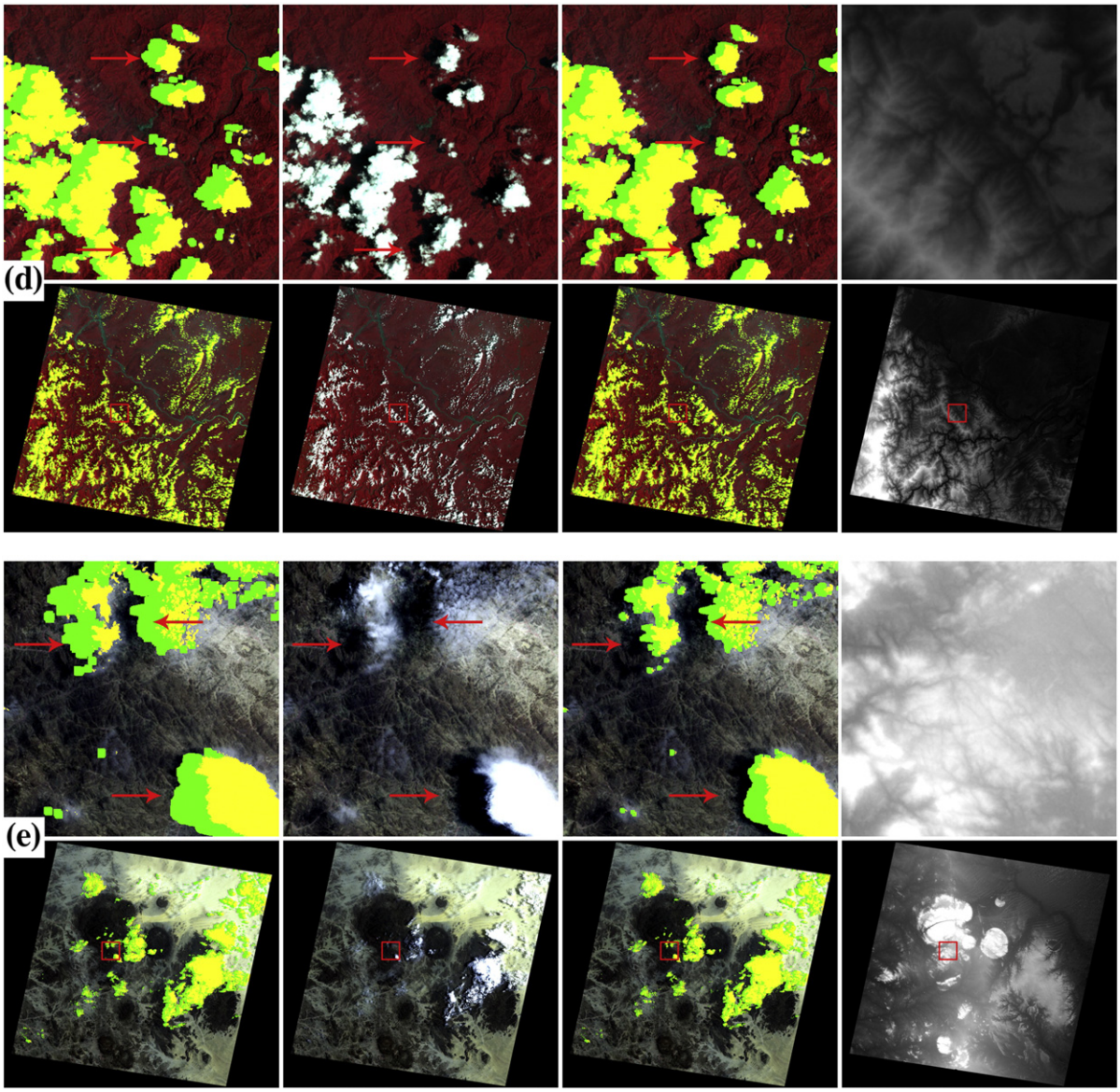

Fig. 11. Comparison of MFmask and Fmask for five Landsat 7 ETM + images from mountainous areas. (a) Located in Himalayas Mountains, Kaski, Nepal (p142_r40 and 19990924). (b) Located at Alps Mountains, Bergamo, Italy (p193_r28 and 20030401). (c) Located at Caucasus Mountains, Chereksky, Kabardino-Balkar Republic (p171_r30 and 20011127). (d) Located at Longmen Mountains, Sichuan, China (p129_r40 and 20020804). (e) Located at Air Mountains, Agadez, Niger (p189_r47 and 20010805). The upper images in panels a, b, and c are enlargements of the lower entire images with a size of 60 × 60 km^2. The upper images in panels d and e are enlargements of the lower entire images with a size of 15 × 15 km^2. The reference images in panels a, d, and e are shown with Bands 4, 3, and 2 composited. The reference images in panels b and c are shown with Bands 5, 4, and 3 composited. (For interpretation of the references to color in this figure, the reader is referred to the web version of this article.)

4.2. MFmask validations

We have validated the cloud and cloud shadow detection accuracies from MFmask and compared with Fmask. Note that the default Fmask algorithm dilates 3 pixels for both clouds and cloud shadows as a default post-processing to reduce omission errors. In this assessment, as we do not want to let this dilation influence our accuracy, we did not dilate our clouds. However, as cloud shadows are relatively small, we dilated cloud shadows by 3 pixels in our assessment.

4.2.1. Cloud mask validation

The assessment of the cloud masks from MFmask was compared against an accompanying assessment of Fmask based on the same 67 manual cloud masks (Fig. 1). Three different accuracies (Eqs. (13)–(15)) were used to assess their accuracy, including cloud overall accuracy, cloud producer's accuracy, and cloud user's accuracy.

$$\text{Cloud overall accuracy} = \frac{\text{agreement between manual mask and algorithm mask}}{\text{total pixels}} \quad (13)$$

$$\text{Cloud producer}'\text{s accuracy} = \frac{\text{agreement of cloud}}{\text{agreement of cloud} + \text{omission of cloud}} \quad (14)$$

$$\text{Cloud user}'\text{s accuracy} = \frac{\text{agreement of cloud}}{\text{agreement of cloud} + \text{comission of cloud}} \quad (15)$$

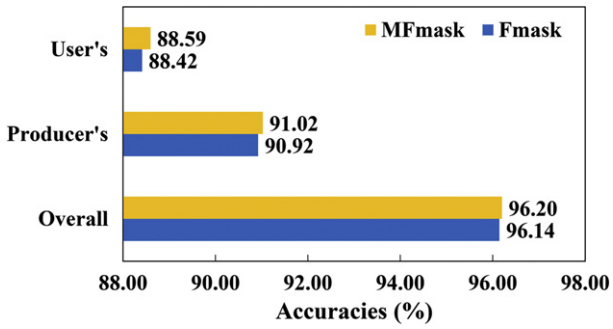

Fig. 12. Average cloud accuracies between MFmask and Fmask.

At the pixel level, the average overall accuracy of the MFmask algorithm is 96.20%, which is 0.06% higher than Fmask (96.14%) (Fig. 12). For cloud cover less than 5%, cloud producer's and user's accuracies were not analyzed, as they will be greatly influenced by the boundary pixels. The average cloud producer's accuracy of MFmask is 91.02%, which is slightly higher than that of Fmask at 90.92% (Fig. 12). Moreover, the average cloud user's accuracy of MFmask is 88.59%, which is also better than Fmask (88.42%) (Fig. 12).

Though the MFmask algorithm shows better accuracies in cloud detection, the improvement is less than what we have expected. This is mostly because MFmask will only show better results than Fmask when there is a strong negative relationship between BT and DEMs. However, there are many times when the lapse rate is close or equal to 0 °C km^{-1} (Fig. 13). The slope of the relationship is smaller or even sometimes positive (higher DEM has higher BT), as other factors (e.g., surface condition, air moisture content, and wind speed) can also influence the temperature (Kattel et al., 2013). In this specific case, MFmask will obtain an insignificant lapse rate and produce a similar cloud mask to Fmask. Fig. 14 shows one Landsat 7 ETM+ image where pixels with higher elevation present higher temperature than pixels with relatively lower elevation. Although the linear model can be built in this case, the estimated lapse rate is more than 0 °C km^{-1}, which will be set to be 0 °C km^{-1} (no normalization) making MFmask produce the same results as Fmask. Additionally, the observed cloud detection improvements from MFmask are also affected by cloud cover condition. For example, if cloud cover is extremely high, there may not be enough clear-sky pixels for MFmask to robustly estimate the lapse rate, particularly when the clear-sky pixels are located in relatively flat areas.

To better demonstrate the improvements, we conducted another comparison between MFmask and Fmask cloud results for all images where the two algorithms differ by more than 0.5%. Fig. 15 shows that if there are large disagreements between the two methods, MFmask shows substantially higher accuracies, except for two images in

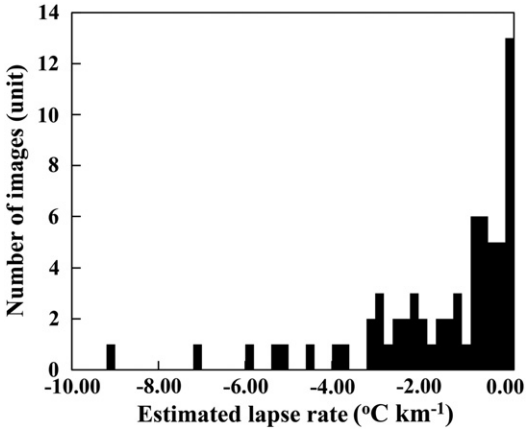

Fig. 13. Histogram of the estimated lapse rates for the 67 reference images.

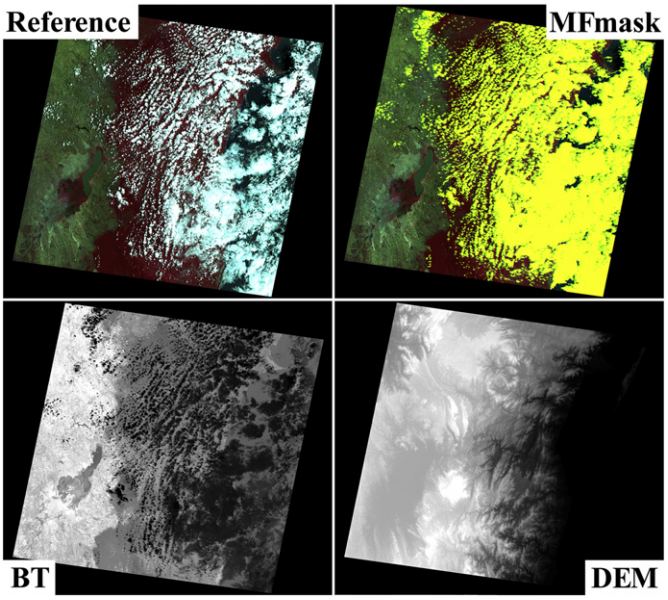

Fig. 14. MFmask results for the Landsat 7 ETM+ image (p158_r72 and 20011116) where the temperature is positively related to the elevation. The upper left image shows the false color composited Landsat image (Bands 4, 3, and 2). The upper right image shows the MFmask cloud (yellow) and cloud shadow (green) mask. The lower left image shows the thermal band (BT). The lower right image shows the corresponding DEM data. (For interpretation of the references to color in this figure legend, the reader is referred to the web version of this article.)

southern Chile (p230_r94 and p229_r97). By carefully checking the manual cloud masks of the two images, we found that the manual masks for the two images are not accurate, as many clouds are not identified in the manual masks.

4.2.2. Cloud shadow mask validation

The validation of the cloud shadow detection was conducted using all 15 reference images with manual cloud shadow masks (Fig. 1). Two different accuracies (Eqs. (16) and (17)) were used to assess the accuracy of MFmask cloud shadow results, including producer's and user's accuracy. Due to the small size of cloud shadows, the cloud shadow overall accuracy was not used for accuracy assessment.

$$\text{Cloud shadow producer's accuracy} = \frac{\text{agreement of cloud shadow}}{\text{agreement of cloud shadow} + \text{omission of cloud shadow}} \quad (16)$$

$$\text{Cloud shadow user's accuracy} = \frac{\text{agreement of cloud shadow}}{\text{agreement of cloud shadow} + \text{comission of cloud shadow}} \quad (17)$$

Table 2 shows the validation of MFmask and Fmask cloud shadow results. The cloud shadow masks created by MFmask provide continuously higher producer's and user's accuracies in all tested images (Table 2). The average cloud shadow producer's accuracy of MFmask is 89.35%, which is a substantial improvement over Fmask (86.64%). At the same time, the average cloud shadow user's accuracy of MFmask is 35.90%, which is also a substantial improvement over Fmask (31.23%). Note that the relatively lower user's accuracy for cloud shadow is mainly caused by the 3 pixels' buffer in both algorithms.

5. Discussions and conclusion

This study presented a new method (MFmask) for detecting cloud and cloud shadow by integrating DEMs into the original Fmask algorithm, which aims to improve the Fmask results for mountainous areas. The MFmask algorithm made several improvements in cloud

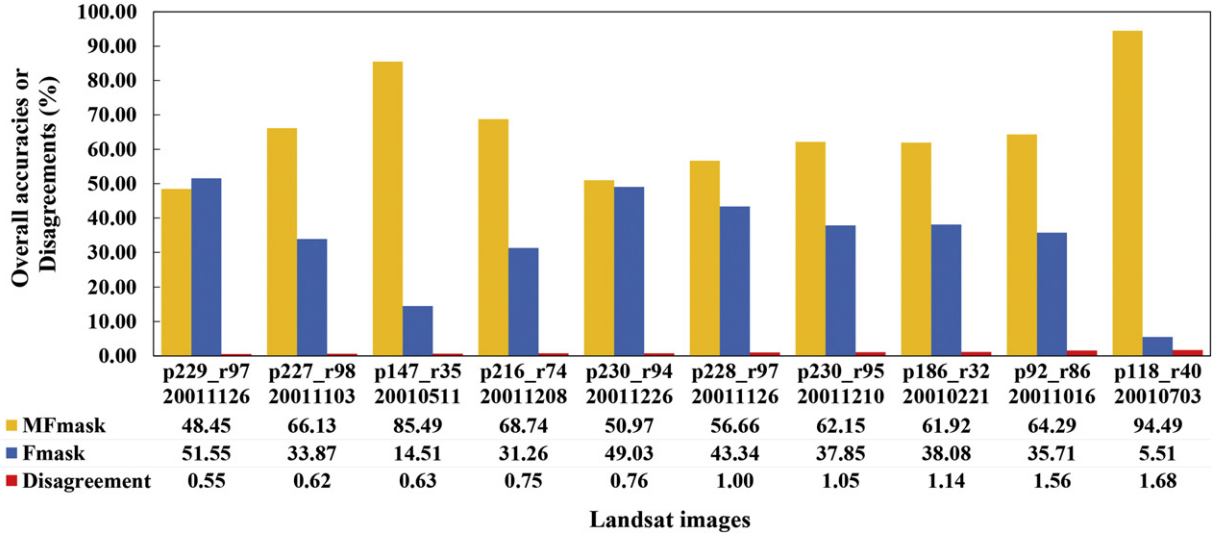

Fig. 15. The cloud detection overall accuracies between MFmask and Fmask for all images with disagreement more than 0.5%. The red bars are the percentage of disagreement between MFmask and Fmask results. The yellow bars are the MFmask overall accuracies, and the blue bars are the Fmask overall accuracies. (For interpretation of the references to color in this figure legend, the reader is referred to the web version of this article.)

and cloud shadow detection based on the original Fmask algorithm for mountainous areas.

For cloud detection, the Fmask algorithm detects cloud over land and water separately, but the water mask in Fmask may be confused with terrain shadows because of their similar spectral response. To address this problem, a slope rule was applied to exclude most of terrain shadows out of a water mask. Moreover, a linear lapse rate model was used to alleviate temperature variations along elevation gradients in cloud detection. The Fmask algorithm assumes the temperature from all clear-sky land pixels in one Landsat image is approximately the same, and this assumption is reasonable for flat areas, but is not valid for mountainous areas. The MFmask algorithm employed a linear lapse rate mode to normalize BT, reducing its variations caused by elevation change in mountainous areas. However, the weak or positive relationship between temperature and elevation sometimes may result in a meaningless lapse rate (approximately 0 °C km^{-1} or greater), as it is also influenced by other factors (e.g., cloud cover condition and surface condition). In those specific cases, MFmask will not trigger the BT normalization process, and generate almost the same cloud masks as Fmask does. This approach not only performs well in mountainous areas, but it is also workable over the relatively flat terrain where minor elevation differences will result in a lapse rate at near-zero level (no BT normalization).

For cloud shadow detection, a double-projection approach was designed to provide more accurate prediction of cloud shadow shape. The prediction of cloud shadow in the original Fmask method assumes that a cloud and its shadow have a similar shape, but it cannot handle the shape change of cloud shadow on slope side. MFmask projects cloud shadow onto the reference plane, and later back projects it into Landsat image based on a DEM derived pixel-location table. This double-projection approach can handle the shape change of cloud shadow on slope side and predict cloud shadow shape more accurately. Additionally, a topographic correction model and an estimated cloud height with neighboring clouds were used to improve the prediction of cloud shadow location. The Fmask algorithm may inaccurately calculate cloud shadow location due to confusion with dark features (e.g., terrain shadows, lakes, and wetlands). In the MFmask algorithm, terrain shadows were removed out of potential cloud shadows by applying the SCS + C correction to the NIR and SWIR bands. Meanwhile, an estimated cloud base height with neighboring clouds was used to reduce the mismatch contributed by other dark features. This approach can also improve cloud shadow detection for non-mountains Landsat images containing dark features other than terrain shadows, such as lakes and wetlands. Those improvements in MFmask lead to consistent increases in the accuracies of the cloud shadow detection compared with Fmask (Table 2). Moreover, the improvements of MFmask are generally larger under lower sun elevation conditions when the cloud

Table 2
MFmask and Fmask cloud shadow detection accuracies.

Landsat images			Producer's accuracies		User's accuracies	
Date	Path/Row	Sun elevation (°)	MFmask	Fmask	MFmask	Fmask
20010205	p1_r75	55.37	79.12%	78.40%	27.91%	23.14%
20010324	p26_r46	57.00	95.09%	93.38%	20.23%	18.21%
20010615	p31_r43	66.29	95.04%	93.93%	54.13%	48.55%
20010814	p35_r42	62.20	94.34%	91.32%	18.98%	17.98%
20010613	p49_r22	55.96	93.96%	91.96%	42.68%	32.98%
20011029	p71_r87	51.87	93.32%	90.19%	42.14%	40.12%
20011103	p74_r91	49.04	89.09%	84.81%	13.24%	12.64%
20010703	p118_r40	65.82	94.09%	89.94%	20.21%	17.14%
20010803	p143_r21	48.95	96.53%	92.67%	39.45%	35.48%
20010422	p158_r72	46.98	94.79%	88.03%	26.26%	24.82%
20011111	p171_r82	58.60	88.19%	85.88%	48.72%	41.89%
20010805	p189_r47	62.92	58.32%	55.88%	52.18%	47.68%
20010511	p195_r26	55.42	85.45%	83.18%	47.62%	40.34%
20011226	p230_r92	51.62	93.38%	92.59%	39.10%	29.64%
20011226	p230_r94	49.91	89.60%	87.46%	45.59%	37.91%
Average			89.35%	86.64%	35.90%	31.23%

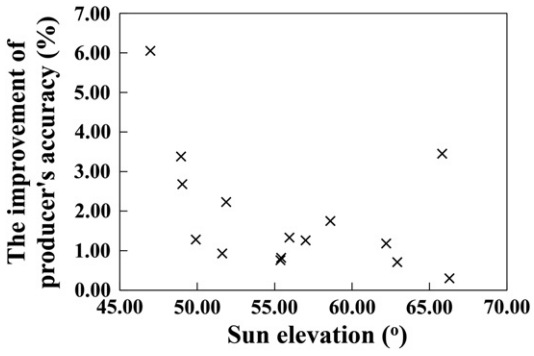

Fig. 16. The improvement of producer's accuracy of cloud shadow detection of MFmask versus sun elevation for the 15 reference images with manual cloud shadow masks.

shadow shape and location are more sensitive to mountainous topography (Fig. 16).

Accuracy assessment was conducted using a total of 67 Landsat reference images covering mountainous areas, where the cloud masks generated by MFmask are slightly better than Fmask (Fig. 12), with a cloud overall accuracy of 96.20% (96.14% in Fmask), cloud producer's accuracy of 91.02% (90.92% in Fmask), and cloud user's accuracy of 88.59% (88.42% in Fmask). In another comparison based on 10 images where the two algorithms yield large differences, MFmask shows substantially higher accuracies (Fig. 15). Moreover, MFmask achieves much better cloud shadow detection accuracies than Fmask for the tested 15 mountainous reference images (Table 2). Overall, these results demonstrate the importance of integrating DEM data in designing cloud and cloud shadow detection algorithms, especially for mountainous areas.

Although MFmask has improved cloud and cloud shadow detection of Landsat images in mountainous areas, this new method still has some limitations. First, the cloud mask produced by MFmask is not always better than Fmask, mainly because the BT normalization of MFmask may decrease the temperature probability of the cloud pixels located in relatively high elevation. This artifact is mostly noticeable for cloud edge pixels, which are influenced by the neighboring warm surface pixels. These minor omission errors may not be that important, as a 3-pixel dilation for cloud mask is recommended in the final applications. Second, MFmask still has the same limitation as Fmask that other very bright and cold land features (e.g., high elevation snow/ice) may be identified as clouds, resulting in incorrect cloud shadows (Selkowitz and Forster, 2015). Although MFmask can reduce the commission errors for the high elevation cloud-like pixels (Fig. 11c), it may also induce more commission errors when those cloud-like pixels are in low elevation compared with the original Fmask (see red arrow in Fig. 17). This is because that the BT normalization also increased the temperature probability of the pixels in lower elevations.

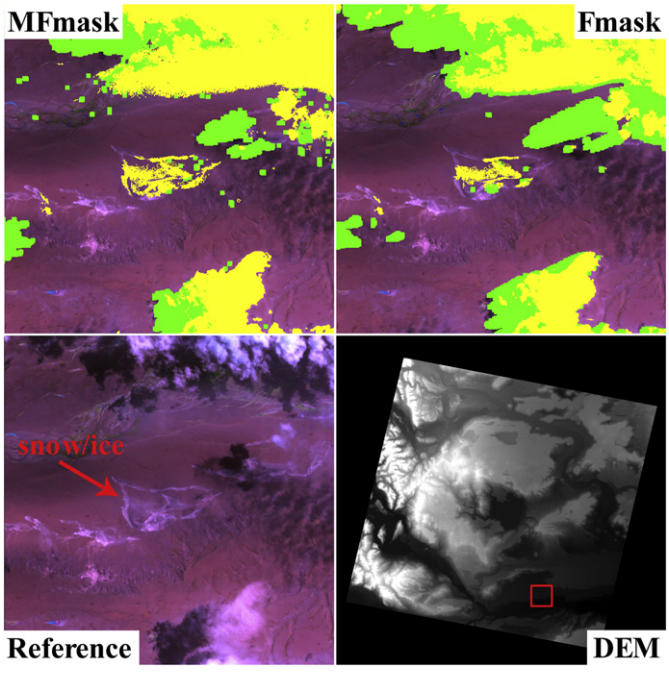

Fig. 17. Comparison of MFmask and Fmask for a subset Landsat 7 ETM+ image from Andes Mountains, Santa Cruz, Argentina (p230_r94 and 20011226) where more commissions of snow/ice as clouds were observed at a relatively low elevation by MFmask. The upper left image shows the MFmask cloud (yellow) and cloud shadow (green) mask for the enlargement of the entire Landsat image with a size of 15 × 15 km^2. The upper right image shows the corresponding Fmask cloud and cloud shadow mask. The lower left image shows the false color composited Landsat image (Bands 5, 4, and 3). The lower right image shows the corresponding DEM data of the entire Landsat image. The red arrow points to the commission errors of snow/ice as clouds in the two algorithms as example. (For interpretation of the references to color in this figure legend, the reader is referred to the web version of this article.)

The ASTER DEM data were used as the source for extracting DEMs in this study for its global coverage at a resolution of 1 arc-second by 1 arc-second (30 by 30 m at equator). However, the ASTER DEM data contains missing data (Tachikawa et al., 2011), which will cause problems for cloud and cloud shadow detection. When many clear-sky land pixels lacking valid DEM data, the cloud detection accuracies may decrease as their BT cannot be effectively normalized. Moreover, if cloud shadows are located at the pixels with lack of DEMs, MFmask may fail to improve the cloud shadow detection, because the shape and the location of cloud shadow cannot be accurately obtained. Therefore, other DEM datasets can be used as the supplement of the ASTER DEM data. For example, the Shuttle Radar Topography Mission (SRTM) 1 arc-second DEM product is recommended for the middle or lower latitude areas because of its higher overall accuracy (Hirt et al., 2010). Additionally, the corresponding DEM data for each Landsat image needs to be manually downloaded, mosaicked, projected, and resampled to Landsat's resolution and extent, so MFmask is inherently more complicated to use compared with Fmask.

To facilitate the use of the MFmask algorithm, we have released a Matlab package (available from https://github.com/qsly09/mfmask/). The time required for this software to process one Landsat image depends on cloud cover and its underlying surface. Generally, the runtime per image, on a 2.0 GHz development computer with an Intel Xeon E5-2650 processor and 24 GB of RAM, is between 1 and 15 min.

In conclusion, we proposed a new algorithm (MFmask) that effectively improves the detection of cloud and cloud shadow for Landsats 4–8 images in mountainous areas by incorporating a DEM into the Fmask algorithm. Compared with Fmask, this new algorithm can produce better cloud and cloud shadow masks for mountainous areas, and can also work well for non-mountainous areas.

Acknowledgments

This study was funded by National Natural Science Foundation of China (Contract #41471293 & 41671361), the Fund Project of Sichuan Provincial Academician (Expert) Workstation (Contract #2014YSGZZ02), and USGS Great Plains Cooperative Ecosystem Studies Unit (CESU) Program (Contract #G17AC00057). Landsat data are courtesy of USGS. ASTER GDEM2 data are downloaded from LP DAAC (NASA Land Data Products and Services). We are also grateful for valuable comments from three anonymous reviewers.

References

Asner, G.P., 2001. Cloud cover in Landsat observations of the Brazilian Amazon. Int. J. Remote Sens. 22 (18), 3855–3862.
Berendes, T., Sengupta, S.K., Welch, R.M., Wielicki, B.A., Navar, M., 1992. Cumulus cloud base height estimation from high spatial resolution Landsat data: a hough transform approach. IEEE Trans. Geosci. Remote Sens. 30 (3), 430–443.
Braaten, J.D., Cohen, W.B., Yang, Z., 2015. Automated cloud and cloud shadow identification in Landsat MSS imagery for temperate ecosystems. Remote Sens. Environ. 169, 128–138.
Choi, H., Bindschadler, R., 2004. Cloud detection in Landsat imagery of ice sheets using shadow matching technique and automatic normalized difference snow index threshold value decision. Remote Sens. Environ. 91 (2), 237–242.
Cohen, W.B., Yang, Z., Kennedy, R., 2010. Detecting trends in forest disturbance and recovery using yearly Landsat time series: 2. TimeSync - tools for calibration and validation. Remote Sens. Environ. 114 (12), 2911–2924.
Colstoun, E.C.B.D., Story, M.H., Thompson, C., Commisso, K., Smith, T.G., Irons, J.R., 2003. National Park vegetation mapping using multitemporal Landsat 7 data and a decision tree classifier. Remote Sens. Environ. 85 (3), 316–327.
Coulter, L.L., Stow, D.A., Tsai, Y.H., Ibanez, N., Shih, H.C., Kerr, A., Benza, M., Weeks, J.R., Mensah, F., 2016. Classification and assessment of land cover and land use change in southern Ghana using dense stacks of Landsat 7 ETM+ imagery. Remote Sens. Environ. 184, 396–409.
Fisher, A., Flood, N., Danaher, T., 2016. Comparing Landsat water index methods for automated water classification in eastern Australia. Remote Sens. Environ. 175, 167–182.
Foga, S., Scaramuzza, P.L., Guo, S., Zhu, Z., Dilley, R.D., Beck, J.T., et al., 2017. Cloud detection algorithm comparison and validation for operational Landsat data products. Remote Sens. Environ. 194, 379–390.

Gao, F., Masek, J., Schwaller, M., Hall, F., 2006. On the blending of the Landsat and MODIS surface reflectance: predicting daily Landsat surface reflectance. IEEE Trans. Geosci. Remote Sens. 44 (8), 2207–2218.
Gao, T., Zhu, J., Zheng, X., Shang, G., Huang, L., Wu, S., 2015. Mapping spatial distribution of larch plantations from multi-seasonal Landsat-8 OLI imagery and multi-scale textures using random forests. Remote Sens. 7 (2), 1702–1720.
Hagolle, O., Huc, M., Pascual, D.V., Dedieu, G., 2010. A multi-temporal method for cloud detection, applied to FORMOSAT-2, VENμS, LANDSAT and SENTINEL-2 images. Remote Sens. Environ. 114 (8), 1747–1755.
He, B., Quan, X., Xing, M., 2013. Retrieval of leaf area index in alpine wetlands using a two-layer canopy reflectance model. Int. J. Appl. Earth Obs. Geoinf. 21, 78–91.
Hermosilla, T., Wulder, M.A., White, J.C., Coops, N.C., Hobart, G.W., 2015. An integrated Landsat time series protocol for change detection and generation of annual gap-free surface reflectance composites. Remote Sens. Environ. 158, 220–234.
Hirt, C., Filmer, M.S., Featherstone, W.E., 2010. Comparison and validation of the recent freely available ASTER-GDEM ver1, SRTM ver4. 1 and GEODATA DEM-9S ver3 digital elevation models over Australia. Aust. J. Earth Sci. 57 (3), 337–347.
Huang, C., Thomas, N., Goward, S.N., Masek, J.G., Zhu, Z., Townshend, J.R., Vogelmann, J.E., 2010a. Automated masking of cloud and cloud shadow for forest change analysis using Landsat images. Int. J. Remote Sens. 31 (20), 5449–5464.
Huang, C., Goward, S.N., Masek, J.G., Thomas, N., Zhu, Z., Vogelmann, J.E., 2010b. An automated approach for reconstructing recent forest disturbance history using dense landsat time series stacks. Remote Sens. Environ. 114 (1), 183–198.
Irish, R.R., 2000. Landsat 7 automatic cloud cover assessment. Proceedings of SPIE - The International Society for Optical Engineering. 4049:pp. 348–355. http://dx.doi.org/10.1117/12.410358.
Irish, R.R., Barker, J.L., Goward, S.N., Arvidson, T., 2006. Characterization of the Landsat-7 ETM+ automated cloud-cover assessment (ACCA) algorithm. Photogramm. Eng. Remote. Sens. 72 (10), 1179–1188.
Jin, S., Homer, C., Yang, L., Xian, G., Fry, J., Danielson, P., Townsend, P.A., 2013. Automated cloud and shadow detection and filling using two-date Landsat imagery in the USA. Int. J. Remote Sens. 34 (5), 1540–1560.
Ju, J., Roy, D.P., 2008. The availability of cloud-free Landsat ETM+ data over the conterminous United States and globally. Remote Sens. Environ. 112 (3), 1196–1211.
Kattel, D.B., Yao, T., Yang, K., Tian, L., Yang, G., Joswiak, D., 2013. Temperature lapse rate in complex mountain terrain on the southern slope of the central Himalayas. Theor. Appl. Climatol. 113 (3), 671–682.
Kennedy, R.E., Yang, Z., Cohen, W.B., 2010. Detecting trends in forest disturbance and recovery using yearly Landsat time series: 1. LandTrendr - temporal segmentation algorithms. Remote Sens. Environ. 114 (12), 2897–2910.
Li, A., Jiang, J., Bian, J., Deng, W., 2012. Combining the matter element model with the associated function of probability transformation for multi-source remote sensing data classification in mountainous regions. ISPRS J. Photogramm. Remote Sens. 67, 80–92.
Lookingbill, T.R., Urban, D.L., 2003. Spatial estimation of air temperature differences for landscape-scale studies in montane environments. Agric. For. Meteorol. 114 (3), 141–151.
Lu, S., Wu, B., Yan, N., Wang, H., 2011. Water body mapping method with HJ-1A/B satellite imagery. Int. J. Appl. Earth Obs. Geoinf. 13 (3), 428–434.
Munroe, D.K., Southworth, J., Tucker, C.M., 2004. Modeling spatially and temporally complex land-cover change: the case of western Honduras. Prof. Geogr. 56 (4), 544–559.
NASA JPL, 2009. ASTER Global Digital Elevation Model [Data set]. NASA JPL. http://dx.doi.org/10.5067/aster/astgtm.002.
Oreopoulos, L., Wilson, M.J., VáRnai, T., 2011. Implementation on landsat data of a simple cloud-mask algorithm developed for modis land bands. IEEE Geosci. Remote Sens. Lett. 8 (4), 597–601.
Quan, X., He, B., Li, X., 2015. A Bayesian network-based method to alleviate the ill-posed inverse problem: a case study on leaf area index and canopy water content retrieval. IEEE Trans. Geosci. Remote Sens. 53 (12), 6507–6517.
Reese, H., Olsson, H., 2011. C-correction of optical satellite data over alpine vegetation areas: a comparison of sampling strategies for determining the empirical c -parameter. Remote Sens. Environ. 115 (6), 1387–1400.
Roy, D.P., Ju, J., Kline, K., Scaramuzza, P.L., Kovalskyy, V., Hansen, M., Loveland, T.R., Vermote, E., Zhang, C., 2010. Web-enabled Landsat data (WELD): Landsat ETM+ composited mosaics of the conterminous United States. Remote Sens. Environ. 114 (1), 35–49.
Sandholt, I., Rasmussen, K., Andersen, J., 2002. A simple interpretation of the surface temperature/vegetation index space for assessment of surface moisture status. Remote Sens. Environ. 79 (2), 213–224.
Scaramuzza, P.L., Bouchard, M.A., Dwyer, J.L., 2012. Development of the Landsat data continuity mission cloud-cover assessment algorithms. IEEE Trans. Geosci. Remote Sens. 50 (4), 1140–1154.
Schroeder, T.A., Wulder, M.A., Healey, S.P., Moisen, G.G., 2011. Mapping wildfire and clearcut harvest disturbances in boreal forests with Landsat time series data. Remote Sens. Environ. 115 (6), 1421–1433.
Selkowitz, D., Forster, R., 2015. An automated approach for mapping persistent ice and snow cover over high latitude regions. Remote Sens. 8 (1), 16.
Soenen, S., Peddle, D.R., Coburn, C., 2005. SCS+ C: a modified sun-canopy-sensor topographic correction in forested terrain. IEEE Trans. Geosci. Remote Sens. 43 (9), 2148–2159.
Tachikawa, T., Hato, M., Kaku, M., Iwasaki, A., 2011. Characteristics of ASTER GDEM version 2. IEEE International Geoscience and Remote Sensing Symposium (IGARSS), pp. 3657–3660.
Teillet, P.M., Guindon, B., Goodenough, D.G., 1982. On the slope-aspect correction of multispectral scanner data. Can. J. Remote. Sens. 8 (2), 84–106.
Verpoorter, C., Kutser, T., Tranvik, L., 2012. Automated mapping of water bodies using Landsat multispectral data. Limnol. Oceanogr. Methods 10, 1037–1050.
Wang, B., Ono, A., Muramatsu, K., Fujiwara, N., 1999. Automated detection and removal of clouds and their shadows from Landsat TM images. IEICE Trans. Inf. Syst. 82 (2), 453–460.
Wilson, M.J., Oreopoulos, L., 2013. Enhancing a simple MODIS cloud mask algorithm for the Landsat data continuity mission. IEEE Trans. Geosci. Remote Sens. 51 (2), 723–731.
Yuan, F., Sawaya, K.E., Loeffelholz, B.C., Bauer, M.E., 2005. Land cover classification and change analysis of the Twin Cities (Minnesota) Metropolitan Area by multitemporal Landsat remote sensing. Remote Sens. Environ. 98 (2), 317–328.
Zhang, Y., Guindon, B., Cihlar, J., 2002. An image transform to characterize and compensate for spatial variations in thin cloud contamination of Landsat images. Remote Sens. Environ. 82 (2), 173–187.
Zhu, X., Chen, J., Gao, F., Chen, X., Masek, J.G., 2010. An enhanced spatial and temporal adaptive reflectance fusion model for complex heterogeneous regions. Remote Sens. Environ. 114 (11), 2610–2623.
Zhu, Z., Woodcock, C.E., 2012. Object-based cloud and cloud shadow detection in Landsat imagery. Remote Sens. Environ. 118, 83–94.
Zhu, Z., Wang, S., Woodcock, C.E., 2015. Improvement and expansion of the Fmask algorithm: cloud, cloud shadow, and snow detection for Landsats 4–7, 8, and Sentinel 2 images. Remote Sens. Environ. 159, 269–277.
Zhu, Z., Fu, Y., Woodcock, C.E., Olofsson, P., Vogelmann, J.E., Holden, C., Wang, M., Dai, S., Yu, Y., 2016. Including land cover change in analysis of greenness trends using all available Landsat 5, 7, and 8 images: a case study from Guangzhou, China (2000–2014). Remote Sens. Environ. 185, 234–257.